Nonlinear Analysis of Stability and Rotational Accuracy of an Unbalanced Rotor Supported by Aerostatic Journal Bearings

TENGFEI YIN[1], GUOQING ZHANG[2], JIANJUN DU[3], AND SUET TO[1], (Member, IEEE)

[1]State Key Laboratory of Ultra-Precision Machining Technology, Department of Industrial and Systems Engineering, The Hong Kong Polytechnic University, Hong Kong, SAR, China
[2]Guangdong Provincial Key Laboratory of Micro/Nano Optomechatronics Engineering, College of Mechatronics and Control Engineering, Shenzhen University, Shenzhen 518060, China
[3]School of Mechanical Engineering and Automation, Harbin Institute of Technology at Shenzhen, Shenzhen 518055, China

Corresponding author: Suet To (sandy.to@polyu.edu.hk)

ABSTRACT This paper presents the nonlinear analysis of stability and dynamic rotational accuracy of an unbalanced rotor supported by aerostatic journal bearings. A finite element method is utilized with the Runge-Kutta fourth order method to solve the transient Reynolds equation and the rotor dynamics equations simultaneously for the dynamic response analysis of the rotor. The dynamic behavior of the rotor center is analyzed under different rotor masses. It is shown that the dynamic responses of the rotor strongly depend on the rotor mass. The periodic, multi-periodic or quasi-periodic motions are observed as the rotor mass changes. Under a given operating speed, the mass at which the resonance occurs is studied and its relationship with the mass of the rotor at the threshold of instability is found for the first time. The influences of supply pressure, bearing clearance, orifice diameter and eccentric distance on the rotational accuracy, the resonance and instability threshold are also investigated. The result of this study can provide guidance for designing aerostatic bearing rotor systems with required running accuracy and stability.

INDEX TERMS Aerostatic bearings, nonlinear analysis, rotational accuracy, whirl stability.

I. INTRODUCTION

Aerostatic bearings are important mechanical components and have been widely employed in high precision and high speed applications, such as ultra-precision/high speed machine tools, precision instruments, electric motors, and disks [1], [2], because of their high accuracy, low noise, zero friction, and long life [3]. High stability and rotational accuracy are very important for the aerostatic bearings. For example, the motion accuracy of the aerostatic bearing spindle directly affects the surface quality of machined mechanical components in ultraprecision diamond turning [4]. However, the air film between the journal and bearing surface introduces nonlinear effects into the dynamics of rotor systems and the systems may show self-excited instability at high rotational speeds or rotor masses. This kind of

instability is also known as half frequency whirl, which means the rotor vibrates at about half the rotational frequency and with large amplitudes, or even the rotor crashes on the bearing surface [5]. Besides, the rotor has an unbalanced mass inevitably, resulting from manufacturing and installation errors [4], even though dynamic balancing work has been done. This causes centrifugal forces to be generated by the rotating rotor and force the rotor to vibrate [6], which is the main source of the rotor's error motions [7], [8]. These motions reduce rotational accuracy, and the forced vibration may even cause resonance. The self-excited instability and mass unbalance-induced vibration are the major obstacles to the further application of aerostatic bearings. Therefore, it is necessary to investigate the dynamic behavior of an unbalanced rotor supported by aerostatic bearings, which will be beneficial for improving the stability and rotational accuracy by selecting the suitable values of geometric and operation parameters.

The associate editor coordinating the review of this manuscript and approving it for publication was Hassen Ouakad[ID].

IEEE Access™

T. Yin *et al.*: Nonlinear Analysis of Stability and Rotational Accuracy of Unbalanced Rotor Supported by Aerostatic Journal Bearings

Many researchers have investigated the stability of air bearings theoretically and experimentally. The linear theory is widely employed to evaluate the bearing dynamic characteristics and predict the stability. Ausman [9] solved the linearized *ph* solutions to the transient Reynolds equations and the equations of motions simultaneously, determined the threshold point for the half frequency whirl, and finally found that the vibration frequency was equal to half the rotational frequency or slightly smaller at the threshold value. Lund [10] developed a calculation approach to estimate the dynamic characteristics, such as the spring and damping coefficients of the air journal bearing, which was applied to predict the critical speed and the unbalance response. Lihua *et al.* [11] employed a hybrid approach which combined the equivalent coefficient method and the partial derivative method to numerically obtain the damping and stiffness coefficients of air bearings. Al-Bender [12] developed a model based on the linear perturbation approach, which was experimentally proven to be effective in the stability prediction of air journal bearings. Chen *et al.* [13] presented the stability analysis of aerostatic bearings using the perturbation method and analyzed the effects of the positions and numbers of the supply holes on the stability. Yu *et al.* [14] analyzed the dynamic performance of externally pressured air bearings with inherent orifices under the excitation of perturbation forces numerically and experimentally. Most of the existing researches on the stability analysis of aerostatic bearings are based on the linear theory. However, it has been proved that the linearized approach is limited to the prediction of vibrations around the equilibrium position with small amplitudes and fails to realize the accurate prediction of rotor center orbits with large amplitudes [15], [16]. There are also a limited number of studies on the dynamic responses of air bearings by the nonlinear orbit method in which the Reynolds equation and the equations of motions are solved together to gain the transient responses of the bearing system. Colombo *et al.* [17] investigated the radial vibrations of a vertical well-balanced rotor with aerostatic bearings using the nonlinear orbit method and found that there were three kinds of possible responses of the rotor center: point stability, orbital stability, and instability with the increasing rotor mass. Wang and Yau [18] presented the nonlinear vibration analysis of an air bearing spindle with high speed. Kuo *et al.* [19] conducted the bifurcation analysis for a porous air bearing system.

Regarding the rotational accuracy of aerostatic bearings, existing research work has focused largely on the accurate measurement of the error motions and the error separation techniques [20]–[23]; and it has been found that the spindle error motion separation method is able to achieve a sub-nanometer measurement accuracy [24]. However, only a few researchers have investigated the rotational accuracy of aerostatic bearing rotor systems theoretically and numerically. Kim and Kim [25] theoretically analyzed the effects of bearing shape error on static rotational accuracy of the rotor and concluded that the shape error of the bearing, especially for a two-lobe or three-lobe shape, would degrade rotational

accuracy and thus should be avoided. Han *et al.* [26] evaluated the stiffness and damping coefficients of the externally pressurized air bearing using the linear approach and then calculated the orbit of the rotor. Yabe [27], [28] theoretically studied how the rotational accuracy was influenced by manufacturing errors, including the out-of-roundness of the rotor and the size deviation of the orifice in aerostatic journal bearing rotor systems, and found that out-of-roundness played a dominant role in rotational accuracy. Cappa *et al.* [29] built a numerical air film model to calculate the error motion of the rotor and investigated the effects of several machining errors and bearing parameters on rotational accuracy. Cui *et al.* [30] studied the effects of machining errors on the rotational accuracy of a rotor supported by porous aerostatic bearings and concluded that compared with non-flatness errors, waviness errors have a greater impact on bearing rotational accuracy. However, all the above papers focused on the effects of geometric imperfections on the static rotational accuracy of a well-balanced rotor supported by aerostatic bearings at a low rotor speed.

In the existing studies on the numerical simulations of the performance of the aerostatic bearings, the finite element method (FEM) and the finite difference method (FDM) are the most commonly used techniques to solve the Reynolds equation. FEM can be adaptable and convenient for a large variety of geometric shapes compared with FDM. In most of the studies [18], [19], [30], [31], Euler's method (or the first order Runge-Kutta method) was employed to solve the equations of motion of the rotor due to its simplicity. However, Euler's method is a first order numerical approach to solving the differential equations which means that it is only first order accurate. Runge-Kutta methods of high order have been developed to improve the accuracy of the solutions. Among them, the Runge-Kutta fourth order method is the most widely used method which can achieve very high accuracy [32] and will be adopted in this study.

To sum up, the published studies provided insight into the stability and rotational accuracy of air bearing rotor systems. In most of them, the analysis was based on the linear theory without considering mass unbalance, although the air bearing rotor system is nonlinear in nature due to the nonlinearity of the air film pressure [33], [34]. And little attention has been paid to the nonlinear dynamic stability and rotational accuracy of aerostatic bearings. Moreover, rotor mass has a great influence on the dynamic responses of the rotor, and a better dynamic performance can be achieved by changing the rotor mass. However, there is a lack of comprehensive studies focused on variations of dynamic rotational accuracy of an unbalanced rotor supported by aerostatic journal bearings with respect to rotor mass. The aim of this study is therefore to shrink the research gaps by solving the nonlinear Reynolds equation numerically together with the rotor dynamics equations for nonlinear transient analysis of the aerostatic bearing rotor system with mass unbalance, with the rotor in a vertical attitude. The dynamic behavior and rotational accuracy of the rotor are analyzed as the rotor mass increases. The mass
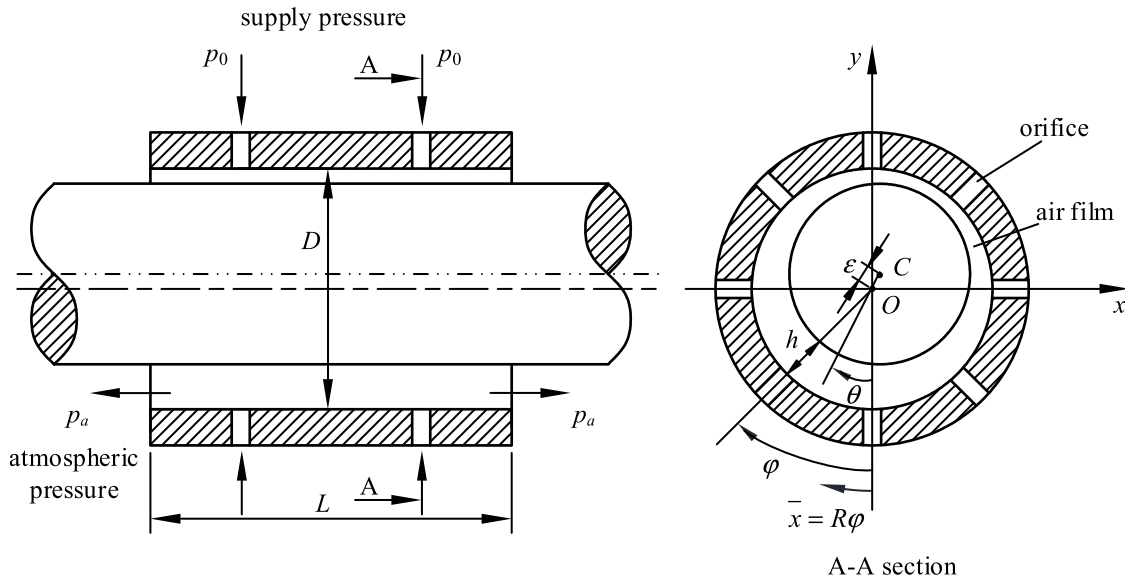
T. Yin *et al.*: Nonlinear Analysis of Stability and Rotational Accuracy of Unbalanced Rotor Supported by Aerostatic Journal Bearings

IEEE *Access*

FIGURE 1. Diagram of the aerostatic journal bearing.

which corresponds to the resonance is investigated for the first time and then the influence of supply pressure, orifice diameter, bearing clearance and eccentric distance on rotational accuracy, resonance and whirl instability are studied. The results of this study will provide useful guidance for designing an aerostatic bearing rotor system and selecting the operating conditions.

II. MATHEMATICAL MODEL

A. REYNOLDS EQUATION

The geometric configuration of an aerostatic journal bearing with inherent orifices is illustrated in Fig. 1. The air with supply pressure p_0 flows into the bearing clearance through the orifices, produces an air film and then flows out from two ends of the bearings with the atmospheric pressure p_a. The air flow in the bearing clearance is modeled by the Reynolds equation, which is derived based on the following assumptions in this study.

1) Due to the ratio of the bearing clearance to the radius of the bearing being very small, and the error resulting from neglecting the curvature is only about 0.1% [35], the curvature of the air film is ignored.
2) The air flow is isothermal, and the rotor and air bearing are rigid.
3) Air viscosity is assumed to be constant, and the value of air pressure keeps constant in the film thickness direction.

Based on the above assumptions, the transient Reynolds equation is derived as:

$$\frac{\partial}{\partial \bar{x}} \left(h^3 \frac{\partial p^2}{\partial \bar{x}} \right) + \frac{\partial}{\partial z} \left(h^3 \frac{\partial p^2}{\partial z} \right) + 24\eta\rho \frac{p_a}{\rho_a} \tilde{v}\delta_i$$
$$= 12\eta u_1 \frac{\partial (ph)}{\partial \bar{x}} + 24\eta \frac{\partial (ph)}{\partial t} \quad (1)$$

where p is the air film pressure, h is the air film thickness, η is the dynamic viscosity of air, z and $\bar{x}$ are the axial and circumferential coordinates, respectively. ρ is the density of air, p_a is the atmospheric pressure, ρ_a is the atmospheric density, $\tilde{v}$ is the velocity flowing through the orifice, u_1 is the velocity in the circumferential direction of the journal surface, $\delta_i = 1$ at the outlet of the orifice in the air film lubrication region, otherwise $\delta_i = 0$.

According to Fig. 1, the thickness of air film can be derived as:

$$h = h_0 + y\cos\varphi + x\sin\varphi \quad (2)$$

where h_0 is bearing clearance, φ is the angular coordinate, $\varphi = \bar{x}/R$, x and y are coordinates of the rotor center C in the x and y directions, respectively.

By using the following expressions:

$$\zeta = \frac{z}{R}, \quad H = \frac{h}{h_0}, \quad P = \frac{p}{p_0}, \quad \bar{Q} = \frac{24\mu R^2 p_a}{h_0^3 p_0^2 \rho_a}\rho\tilde{v},$$

$$\Lambda = \frac{12\eta R^2 \omega}{p_0 h_0^2}, \quad \sigma = \frac{24\eta R^2 \omega}{p_0 h_0^2}, \quad \tau = \omega t, \text{ and } f = P^2$$

where R is the radius of the bearing, p_0 is the supply pressure and ω is the angular velocity of the rotor, the dimensionless form of the Reynolds equation can be obtained:

$$\frac{\partial}{\partial \zeta} \left(H^3 \frac{\partial f}{\partial \zeta} \right) + \frac{\partial}{\partial \varphi} \left(H^3 \frac{\partial f}{\partial \varphi} \right) + \bar{Q}\delta_i$$
$$= \Lambda \frac{\partial (PH)}{\partial \varphi} + \sigma \frac{\partial (PH)}{\partial \tau} \quad (3)$$

The air film pressure distribution, i.e. the solution of (3) must satisfy the following three kinds of boundary conditions:

1) At both ends of the bearing: $P = p_a/p_0$.
2) At the symmetric boundary: $\partial P/\partial n = 0$.

IEEE *Access*

T. Yin *et al.*: Nonlinear Analysis of Stability and Rotational Accuracy of Unbalanced Rotor Supported by Aerostatic Journal Bearings

3) At the orifice: $P = p_d/p_0$.

In this study, the Reynolds equation given in (3) is solved numerically using the finite element method to obtain the air film pressure distribution. Firstly, by applying the Galerkin's weighted residual method, equation (3) is changed as:

$$\iint_\Omega \left[H^3 \left(\frac{\partial f}{\partial \zeta} \frac{\partial \delta f}{\partial \zeta} + \frac{\partial f}{\partial \varphi} \frac{\partial \delta f}{\partial \varphi} \right) - \bar{Q}\delta_i \delta f \right.$$
$$\left. - \Lambda PH \frac{\partial \delta f}{\partial \varphi} + \sigma \frac{\partial (PH)}{\partial \tau}\delta f \right] d\zeta d\varphi = 0 \quad (4)$$

where δf is the variation of f.

Then, equation (4) is discretized in the computational domain by the finite element method. f, H and P can be expressed approximately as:

$$\begin{cases} f = \mathbf{N}^{e\text{T}} \mathbf{f}^e \\ H = \mathbf{N}^{e\text{T}} \mathbf{H}^e \\ P = \mathbf{N}^{e\text{T}} \mathbf{P}^e \end{cases} \quad (5)$$

where superscript e refers to an element, $\mathbf{N}^e$ is the shape function, $\mathbf{f}^e$, $\mathbf{H}^e$ and $\mathbf{P}^e$ are the element vectors consisting of nodal values of the element. In two-dimensional finite element analysis, triangular elements and rectangular elements are commonly used, in which the triangular elements are easier and have the advantages of high calculation accuracy and efficiency in solving the Reynolds equation [35]–[37]. Therefore, triangular elements are adopted in the present analysis.

A vector $\mathbf{Q}^e$ is introduced to link the element vectors with the global vectors, which consists of all the nodal values, let:

$$\begin{cases} \mathbf{f}^e = \mathbf{Q}^e \mathbf{f}_{n\times 1} \\ \delta \mathbf{f}^e = \mathbf{Q}^e \delta \mathbf{f}_{n\times 1} \\ \mathbf{P}^e = \mathbf{Q}^e \mathbf{P}_{n\times 1} \end{cases} \quad (6)$$

where n is the total number of nodes in the computational domain.

By introducing (5) and (6) to (4), the finite element formulation can be derived as:

$$\mathbf{K}\mathbf{f}_{n\times 1} - \Lambda \mathbf{B}\mathbf{P}_{n\times 1} + \sigma \mathbf{C}\mathbf{f}_{n\times 1} + \sigma \mathbf{D}\frac{\partial \mathbf{P}_{n\times 1}}{\partial \tau} = \mathbf{T} \quad (7)$$

where

$$\mathbf{K} = \sum_{e=1}^{n_e} \mathbf{Q}^{e\text{T}} \iint_{\Delta_e} \left(\mathbf{N}^{e\text{T}} \mathbf{H}^e \right)^3 \left(\begin{array}{c} \frac{\partial \mathbf{N}^e}{\partial \zeta} \frac{\partial \mathbf{N}^{e\text{T}}}{\partial \zeta} \\ + \frac{\partial \mathbf{N}^e}{\partial \varphi} \frac{\partial \mathbf{N}^{e\text{T}}}{\partial \varphi} \end{array} \right) d\zeta d\varphi \mathbf{Q}^e \quad (8)$$

$$\mathbf{B} = \sum_{e=1}^{n_e} \mathbf{Q}^{e\text{T}} \frac{\partial \mathbf{N}^e}{\partial \varphi} \mathbf{H}^{e\text{T}} \iint_{\Delta_e} \mathbf{N}^e \mathbf{N}^{e\text{T}} d\zeta d\varphi \mathbf{Q}^e \quad (9)$$

$$\mathbf{C} = \sum_{e=1}^{n_e} \mathbf{Q}^{e\text{T}} \iint_{\Delta_e} \mathbf{N}^e \mathbf{N}^{e\text{T}} \frac{\partial \mathbf{H}^e}{\partial \tau} \mathbf{N}^{e\text{T}} d\zeta d\varphi \mathbf{Q}^e \quad (10)$$

$$\mathbf{D} = \sum_{e=1}^{n_e} \mathbf{Q}^{e\text{T}} \iint_{\Delta_e} \mathbf{N}^e \mathbf{N}^{e\text{T}} \mathbf{H}^e \mathbf{N}^{e\text{T}} d\zeta d\varphi \mathbf{Q}^e \quad (11)$$

$$\mathbf{T} = \sum_{e=1}^{n_e} \mathbf{Q}^{e\text{T}} \iint_{\Delta_e} \bar{Q} \mathbf{N}^e \delta_i d\zeta d\varphi = k_1 \mu_r \dot{m}_r \delta_i \quad (12)$$

n_e is the total number of elements in the computational domain, Δ_e is the area of the element, μ_r is the ratio of the area entering in the computational domain to the total area of the r-th orifice, $\dot{m}_r$ is the mass flow rate of the r-th orifice, and $k_1 = 24\eta p_a/(h_0^3 p_0^2 \rho_a)$.

The ideal air mass flow rate, as derived in [35], is:

$$\dot{m} = A p_0 \phi \sqrt{\frac{2\rho_a}{p_a}} \psi \quad (13)$$

$$\psi = \begin{cases} \left[\frac{\kappa}{2} \left(\frac{2}{\kappa+1} \right)^{(\kappa+1)/(\kappa-1)} \right]^{1/2}; & \frac{p}{p_0} \leq \beta_\kappa \\ \left\{ \frac{\kappa}{\kappa-1} \left[\left(\frac{p}{p_0} \right)^{2/\kappa} - \left(\frac{p}{p_0} \right)^{(\kappa+1)/\kappa} \right] \right\}^{1/2}; & \frac{p}{p_0} > \beta_\kappa \end{cases} \quad (14)$$

where A is the area of the orifice, ϕ is the discharge coefficient, and $\phi = 0.8$, $\kappa = 1.4$ for the ideal air and $\beta_\kappa = \left(\frac{2}{\kappa+1} \right)^{\kappa/\kappa-1}$.

Equation (7) is used to solve the unsteady-state Reynolds equation. A finite element formulation for the steady-state equation can be got as (15) by omitting the time-dependent items.

$$\mathbf{K}\mathbf{f}_{n\times 1} - \Lambda \mathbf{B}\mathbf{P}_{n\times 1} = \mathbf{T} \quad (15)$$

By integrating the air film pressure distribution over the rotor surface, the bearing forces can be gained as:

$$\begin{cases} f_{ax} = p_0 R^2 \int_0^{L/(2R)} d\zeta \int_0^{2\pi} P \sin \varphi d\varphi \\ f_{ay} = p_0 R^2 \int_0^{L/(2R)} d\zeta \int_0^{2\pi} P \cos \varphi d\varphi \end{cases} \quad (16)$$

B. ROTOR DYNAMICS EQUATIONS

In this study, only translational motions in the x and y directions are considered, as illustrated in Fig. 1. And the dynamics equations of the rotor expressed in the coordinate system xoy can be written as:

$$\begin{cases} m\frac{d^2x}{dt^2} = f_{ex} + f_{ax} + mr\omega^2 \cos \omega t \\ m\frac{d^2y}{dt^2} = f_{ey} + f_{ay} + mr\omega^2 \sin \omega t \end{cases} \quad (17)$$

where m is the rotor mass, r is the mass eccentric distance, i.e. the distance between the geometry center and mass center of the rotor, t is time, f_{ex} and f_{ey} are the components of the external forces in the x and y directions, respectively.

By introducing the following dimensionless parameters:

$$X = \frac{x}{h_0}, \quad Y = \frac{y}{h_0}, \quad \bar{r} = \frac{r}{h_0}, \quad F_{ex} = \frac{f_{ex}}{P_0 R^2}, \quad F_{ey} = \frac{f_{ey}}{P_0 R^2},$$

$$F_{ax} = \frac{f_{ax}}{P_0 R^2}, \quad F_{ay} = \frac{f_{ay}}{P_0 R^2}, \quad M = \frac{mh_0\omega^2}{P_0 R^2},$$

T. Yin *et al.*: Nonlinear Analysis of Stability and Rotational Accuracy of Unbalanced Rotor Supported by Aerostatic Journal Bearings

IEEE *Access*

the dimensionless form of (17) is then rewritten as:

$$\begin{cases} M\dfrac{d^2X}{d\tau^2} = F_{ex} + F_{ax} + Mr\cos\tau \\ M\dfrac{d^2Y}{d\tau^2} = F_{ey} + F_{ay} + M\bar{r}\sin\tau \end{cases} \quad (18)$$

C. COMPUTATION PROCEDURE

The pressure distribution of air film obtained by solving (7) is determined by the rotor's position from (18), and at the same time, F_{ax} and F_{ay} in (18) can be calculated by (16), which is related to the air film pressure distribution. This means that the Reynolds equation and the rotor dynamics equations couple. To obtain the rotor's dynamic response under external forces, air film forces and centrifugal forces, equation (7) and equation (18) need to be solved simultaneously.

By introducing the state variables,

$$\psi_1 = X, \quad \psi_2 = \dot{X}, \quad \psi_3 = Y, \quad \psi_4 = \dot{Y}$$

the rotor dynamics equations can be converted into the state equations as follows:

$$\begin{cases} \dfrac{d\psi_1}{d\tau} = \psi_2 \\ \dfrac{d\psi_2}{d\tau} = \dfrac{F_{ex} + F_{ax}}{M} + \bar{r}\cos\tau \\ \dfrac{d\psi_3}{d\tau} = \psi_4 \\ \dfrac{d\psi_4}{d\tau} = \dfrac{F_{ey} + F_{ay}}{M} + \bar{r}\sin\tau \end{cases} \quad (19)$$

The resulting equations for the dynamic response of the rotor are:

$$\dfrac{d\psi_i}{d\tau} = g_i(\tau, \boldsymbol{P}, \psi_1, \psi_2, \psi_3, \psi_4), \quad i = 1, 2, 3, 4$$

$$\dfrac{dP_j}{d\tau} = w_j(\tau, \boldsymbol{P}, \psi_1, \psi_2, \psi_3, \psi_4), \quad j = 1, 2, 3 \ldots n \quad (20)$$

where n is the number of the grid nodes in the computational domain. w_j can be obtained by (7) and the boundary conditions.

Equation (20) can be rewritten for convenience in a vector form as:

$$\dfrac{d\boldsymbol{S}}{d\tau} = \boldsymbol{I}(\tau, \boldsymbol{S}) \quad (21)$$

where $\boldsymbol{S}$ is the vector consisting of $\psi_1, \psi_2, \psi_3, \psi_4$ and $P_1, P_2 \cdots P_n$, and $\boldsymbol{I}$ is the vector consisting of g_1, g_2, g_3, g_4 and $w_1, w_2 \cdots w_n$. The dimensions of $\boldsymbol{S}$ and $\boldsymbol{I}$ are both $(n+4) \times 1$.

The Runge-Kutta fourth order method is a numerical approach to solving the differential equations of the form like (21), with fourth order accuracy. If the same time step is adopted, it has higher accuracy than Euler's method. And thus the Runge-Kutta fourth order method is employed to solve (21) in this study. In this method, the value $\boldsymbol{S}_{k+1}$ at the $(k+1)$-th time step is estimated by the value $\boldsymbol{S}_k$ at the k-th

TABLE 1. Comparison of the load carrying capacity between the results from [38] and those from the present study.

Eccentricity ratio	Load carrying capacity of bearing (N)		
	FDM & Newton iteration [38]	Test [38]	The present model
1/12	7.81	8.48	7.57
2/12	13.65	15.1	13.45
3/12	19.65	22.15	20.06
4/12	25.79	29.78	27.29

time step plus the weighted average of four increments, which is given by:

$$\begin{cases} \boldsymbol{K}_1 = \boldsymbol{I}(\tau_k, \boldsymbol{S}_k) \\ \boldsymbol{K}_2 = \boldsymbol{I}\left(\tau_k + \dfrac{\Delta\tau}{2}, \boldsymbol{S}_k + \Delta\tau\dfrac{\boldsymbol{K}_1}{2}\right) \\ \boldsymbol{K}_3 = \boldsymbol{I}\left(\tau_k + \dfrac{\Delta\tau}{2}, \boldsymbol{S}_k + \Delta\tau\dfrac{\boldsymbol{K}_2}{2}\right) \\ \boldsymbol{K}_4 = \boldsymbol{I}(\tau_k + \Delta\tau, \boldsymbol{S}_k + \Delta\tau\boldsymbol{K}_3) \\ \boldsymbol{S}_{k+1} = \boldsymbol{S}_k + \dfrac{\Delta\tau}{6}(\boldsymbol{K}_1 + 2\boldsymbol{K}_2 + 2\boldsymbol{K}_3 + \boldsymbol{K}_4) \end{cases} \quad (22)$$

where $\Delta\tau$ is the time step size.

The computational procedure of the dynamic response of the rotor is shown in Fig. 2. It starts with a given initial position, i.e. X_0, Y_0 and then the air film pressure distribution can be obtained by solving the steady-state Reynolds equation (15). The bearing forces can be calculated by (16). The initial velocities of the rotor in the x and y directions are assumed to be 0. The displacements and velocities of the rotor and the pressure distribution of air film can be obtained by solving (21) using the Runge-Kutta fourth order method described in (22) step by step. MATLAB is used to solve these equations.

III. RESULTS AND DISCUSSION

In this study, the steady-state Reynolds equation needs to be solved first and then the rotor's dynamic responses can be obtained by combining the transient Reynolds equation and the rotor dynamics equations. To validate the proposed numerical methods and program code, the calculation results from this study are compared with the previous studies.

Table 1 shows the comparison of the load carrying capacity of the aerostatic journal bearing between the results from [38] and those from the present study using the same bearing parameters(D = 25 mm, L = 50 mm, h_0 = 12 μm, d_0 = 0.2 mm), where $F = \sqrt{f_{ax}^2 + f_{ay}^2}$. It is found that the calculated results by the proposed model are in good agreement with both the experimental results and the calculated ones by FDM & Newton iteration in [38]. Compared with FDM & Newton iteration, and the experiment, the maximum errors of the present model are 5% and 11%, which validates the numerical model for the steady-state Reynolds equation in this study.

Fig. 3 illustrates the orbits of a well-balanced rotor with a self-acting air journal bearing. Fig. 3(a) is from [31] where
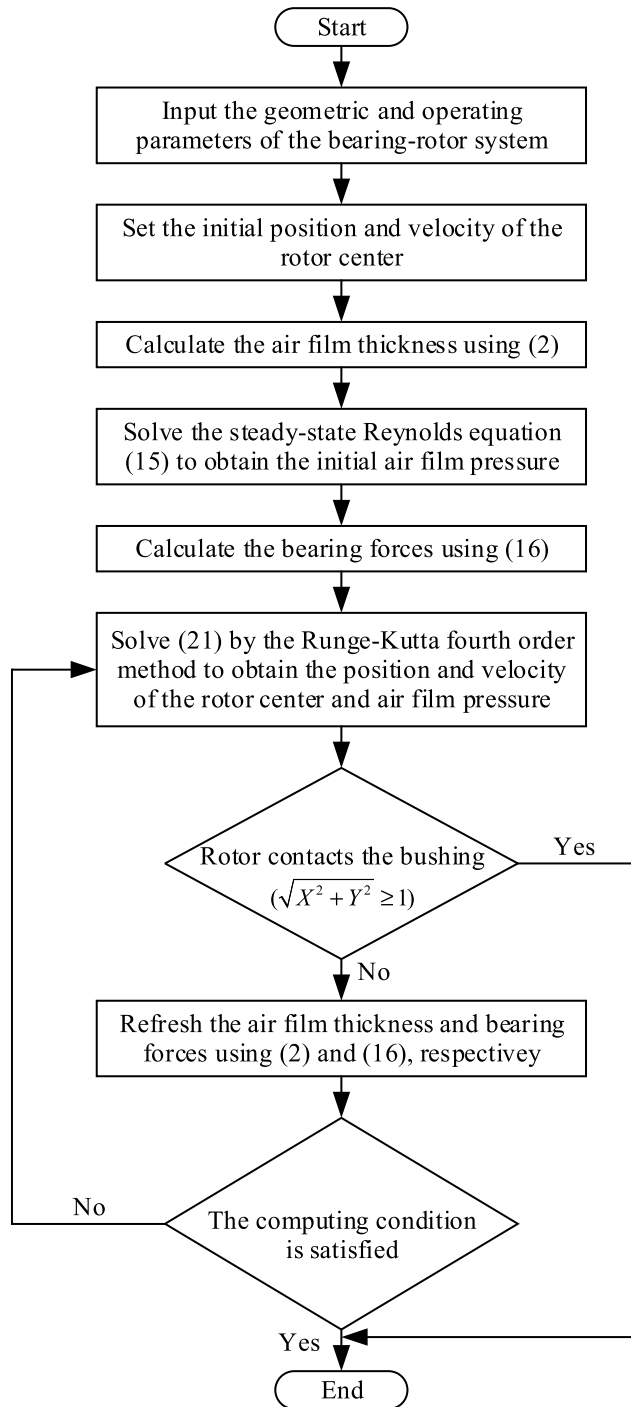
FIGURE 2. The computational flow chart of the dynamic response of the rotor.

TABLE 2. The bearing parameters.

Bearing parameters	Value
Bearing diameter (D)	20 mm
Bearing length (L)	30 mm
Row number of orifices	2
Numbers of orifices for each row	8
Atmospheric pressure (p_a)	1.0×10^5 Pa
Air viscosity (η)	1.8×10^{-5} Pa·s
Heat capacity ratio (κ)	1.4
Rotational speed (n_r)	60000 rpm

In the following study, the transient behaviors of a vertical unbalanced rotor with an aerostatic bearing are investigated as the rotor mass varies. The effects of supply pressure, orifice diameter, bearing clearance and eccentric distance on rotational accuracy and stability are then further studied. The parameters of the bearing rotor system used in this study are given in Table 2.

A. EFFECTS OF ROTOR MASS

To investigate the effects of the rotor mass on the transient behaviors, a series of simulations is carried out for different rotor masses. The orbits of the rotor center, phase portraits, and Poincaré maps are employed to analyze the rotor's dynamic behavior. In addition, fast Fourier transformation (FFT) is used to gain the displacement spectra of the rotor center. In the simulations, supply pressure $p_0 = 0.5$ Mpa, orifice diameter $d_0 = 0.3$ mm, bearing clearance $h_0 = 20 \ \mu$m, and eccentric distance $r = 1 \ \mu$m.

Figs. 4(a) - 6(a) show the orbits of the rotor center at $m = 0.2$ kg, 0.475 kg and 0.48 kg. It can be observed that the orbit of the rotor center is regular for low values of rotor mass ($m = 0.2$ kg). This is different from the transient response of a well-balanced rotor for which the orbit converges to a point at small rotor masses [17]. The regular orbits persist for all rotor masses less than 0.47 kg. The orbit becomes irregular with relatively low amplitudes at $m = 0.475$ kg and loses its stability and fluctuates with large amplitudes (close to 1) at $m = 0.48$ kg.

Figs. 4(b) - 6(b) illustrate the phase portraits of the rotor center at different masses. It is found that the phase portrait at $m = 0.2$ kg is regular and similar to the orbit of the rotor center. But the phase portraits become irregular at $m = 0.475$kg and 0.48 kg.

The FFT spectra of the rotor displacement in the x direction and Poincaré maps are shown in Figs. 4(c, d) - 6(c, d) at $m = 0.2$ kg, 0.475 kg and 0.48 kg. It is clearly seen that the rotor performs harmonic motion with the frequency equal to the rotational frequency of the rotor ($60000/60 = 1000$ Hz) at $m = 0.2$ kg, and one point in the Poincaré map (see Fig. 4(d)) confirms that the motion of the rotor center is a T-periodic motion. By increasing rotor mass, the FFT spectrum shows another peak at about half the rotational frequency (500 Hz) at $m = 0.475$ kg. And discrete points in the Poincaré map indicate a multi-periodic motion. As shown
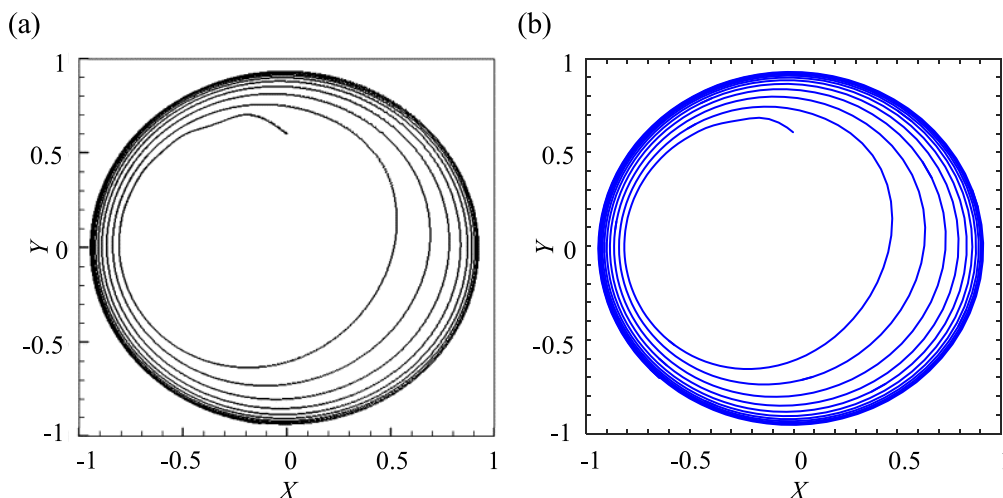
FDM and Euler's method were used. And Fig. 3(b) is the result from the present numerical model by setting the orifice diameter to be 0 for self-acting bearings. As can be seen, the two orbits are very similar, and they both run spirally outwards and finally form a circle whose radius is close to 1. This shows the correctness of the numerical methods for the rotor's dynamic response. Overall, the good agreements with [31], [38] validate the numerical model in this study.

T. Yin *et al.*: Nonlinear Analysis of Stability and Rotational Accuracy of Unbalanced Rotor Supported by Aerostatic Journal Bearings

IEEE *Access*

FIGURE 3. The orbit of the rotor center ($L/D = 1$, $\Lambda = 0.1$, $M = 0.15$, $F_e = 0.1292$) (a) from [31] (Reprinted from [31], Copyright (2009), with permission from Elsevier) and (b) from the present study.
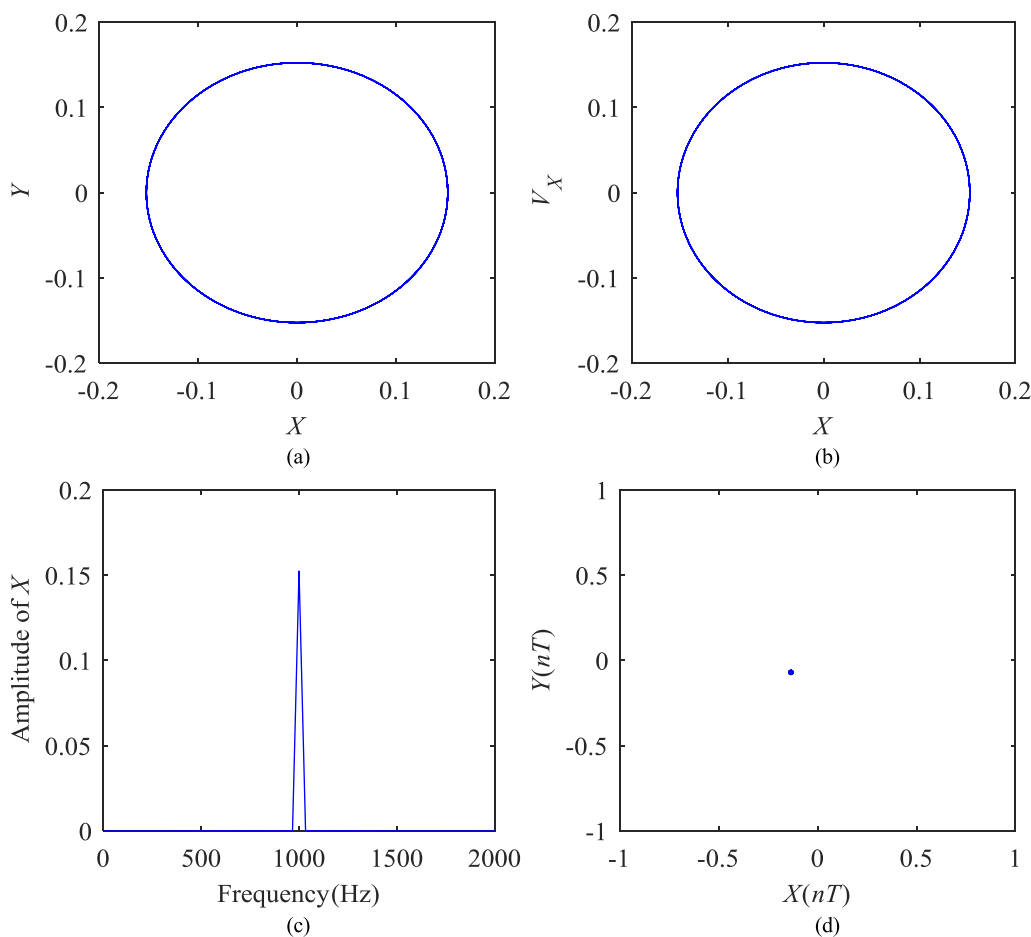

FIGURE 4. Dynamic response, (a) the orbit of rotor center, (b) phase portrait, (c) FFT spectrum of rotor displacement in the *x* direction, (d) Poincaré map at *m* = 0.2 kg.

in Fig. 6(c), the amplitude at half the rotational frequency increases sharply and the closed curve formed in Fig. 6(d) demonstrates quasi-periodic motion at $m = 0.48$ kg.

Fig. 7 shows the waterfall plot of the rotor's responses in the *x* direction. It provides us with the information of amplitudes and frequencies for rotor masses from 0.02 kg to
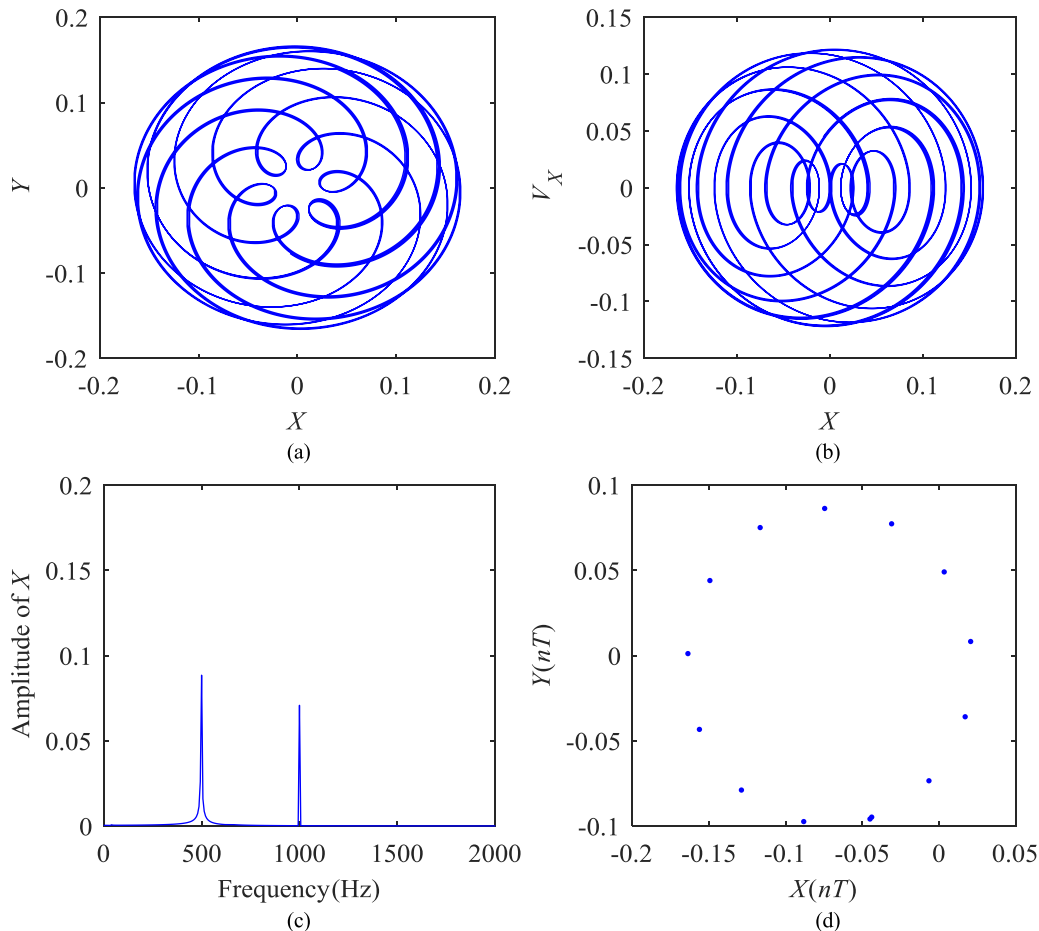
FIGURE 5. Dynamic response, (a) the orbit of rotor center, (b) phase portrait, (c) FFT spectrum of rotor displacement in the *x* direction, (d) Poincaré map at *m* = 0.475 kg.

0.48 kg. It is observed that the synchronous vibration occurs when the rotor mass is below 0.47 kg and the amplitude increases as the rotor mass increases until $m = 0.14$ kg, and then slowly decreases until $m = 0.47$ kg. The rotating unbalanced mass generates the centrifugal force whose direction changes periodically because of the rotation, as a result, the rotor is forced to vibrate at the frequency of the rotational speed. Therefore, the synchronous vibration originates from the unbalanced mass. The stiffness of the bearing can be estimated by $k = \Delta F / \Delta \varepsilon$, and the calculated value is 5.3×10^6 N/m. The natural frequency can be then obtained by $f_n = \sqrt{k/m}/(2\pi)$. It is found that at $m = 0.14$ kg, the estimated natural frequency is 979.25 Hz which is very close to the forcing frequency (rotational frequency) of 1000 Hz. This means that resonance occurs, and thus, the amplitude of synchronous vibration reaches the maximum at $m = 0.14$ kg. And the mass which corresponds to the resonance is denoted as m_r in this study.

The former results have shown that the multi-periodic or quasi-periodic motion occurs at the rotor mass above 0.47 kg. In addition, it can be also observed from Fig. 7 that when the rotor mass is more than 0.47 kg, there is another peak at

about half the rotational frequency of the rotor. This component is called half frequency whirl. To investigate what it comes from, additional simulations of the responses of a well-balanced rotor are conducted to remove the effect of the unbalanced mass, in which the mass eccentric distance $r = 0$ and other parameters are the same as the above simulations. Fig. 8 plots the responses of a well-balanced rotor in the *x* direction at $m = 0.2$ kg and 0.47 kg. It can be observed that the vibration amplitude decreases to 0 after tens of milliseconds, although the FFT spectrum shows a very small peak at the natural frequency of the bearing at $m = 0.2$ kg. However, the half frequency whirl occurs, and its amplitude does not decrease with time and keeps constant when m increases to 0.47 kg. Therefore, it can be inferred that the half frequency whirl originates from the bearing air film itself and this self-excited vibration occurs only if m is larger than a certain value. Moreover, its amplitude grows dramatically under the effect of both air film and unbalanced mass for an unbalanced rotor, as the rotor mass goes beyond 0.47 kg, which indicates an unstable state and is dangerous to the system as shown in Fig. 7. As seen in Fig. 7, the amplitude at $m = 0.48$ kg is very large, and this is probably because
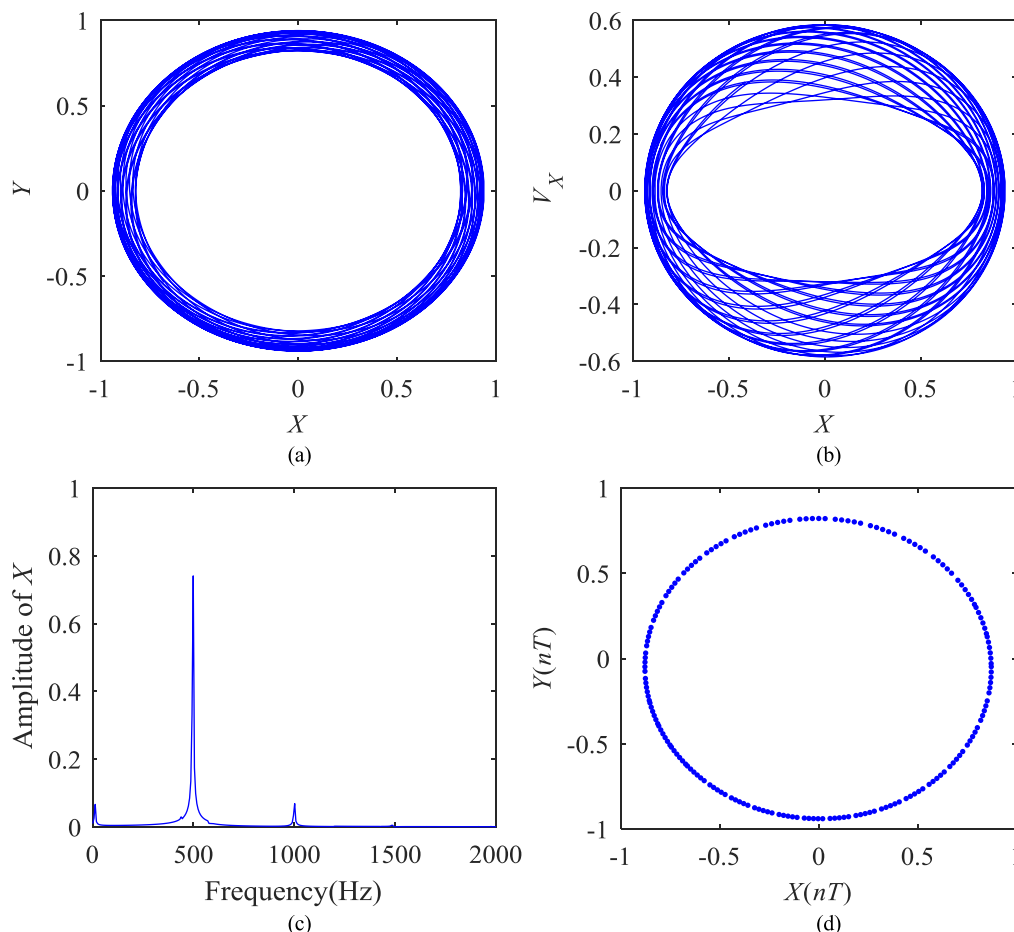
T. Yin *et al.*: Nonlinear Analysis of Stability and Rotational Accuracy of Unbalanced Rotor Supported by Aerostatic Journal Bearings

IEEE *Access*

FIGURE 6. Dynamic response, (a) the orbit of rotor center, (b) phase portrait, (c) FFT spectrum of rotor displacement in the *x* direction, (d) Poincaré map at *m* = 0.48 kg.
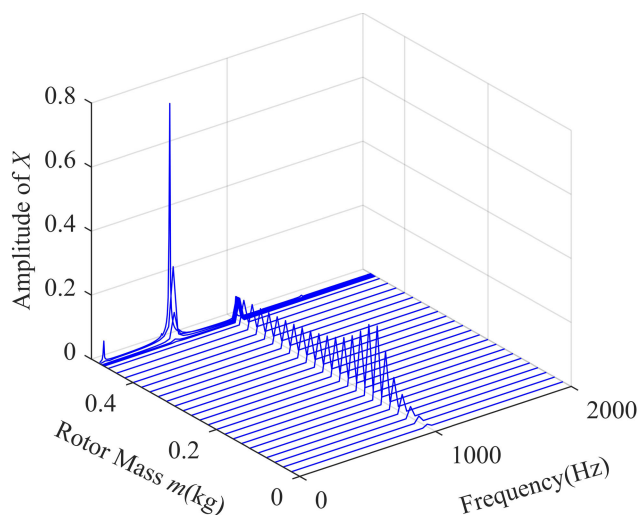

FIGURE 7. Waterfall plot of rotor's responses in the *x* direction.

the natural frequency at m = 0.48 kg is close to half the rotational frequency (ω /2) and it shows good agreement with the value of m_r (0.14 kg) that is approximately a quarter of 0.48 kg. As the rotor mass continues to increase, the rotor

will vibrate at an amplitude of nearly 1 or even crashes on the bearings. In this paper, the mass that starts with half frequency whirl is defined as threshold mass of instability (m_t) and it is slightly smaller than 4 times the mass which corresponds to the resonance (m_r) under the same operating speed.

B. EFFECTS OF SUPPLY PRESSURE

An analysis is conducted of the effects of supply pressure on rotational accuracy, the resonance and instability threshold of the rotor. The rotational accuracy is studied by investigating the amplitudes of the rotor center orbits. In the simulations, orifice diameter d_0 = 0.2 mm, bearing clearance h_0 = 20 μm, and eccentric distance r = 1 μm.

Fig. 9 illustrates the variations of rotational accuracy with respect to the rotor mass less than the threshold mass of instability (m_t) for different supply pressures. It should be noted that the m_t varies with different supply pressures. It is shown that with the growth of the rotor mass, the orbit amplitudes increase first and then decrease for all supply pressures. This shows good agreement with the former results. The influence of supply pressure on the resonance is obvious, that the larger supply pressure can delay the resonance. This
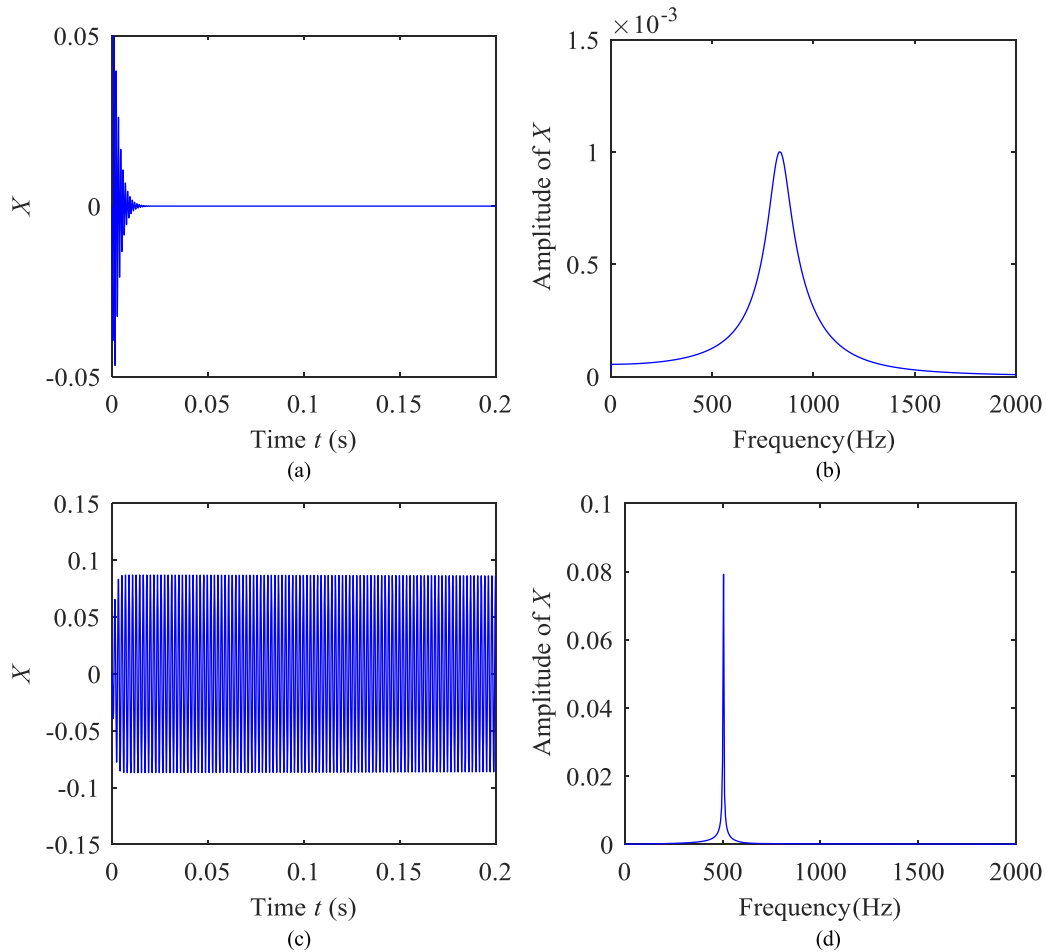
IEEE *Access*

T. Yin *et al.*: Nonlinear Analysis of Stability and Rotational Accuracy of Unbalanced Rotor Supported by Aerostatic Journal Bearings

FIGURE 8. Dynamic response of a well-balanced rotor, (a) and (c) time response in the *x* direction at *m* = 0.2 kg and 0.47 kg, respectively; (b) and (d) FFT spectra of rotor displacement in the *x* direction *m* = 0.2 kg and 0.47 kg, respectively.
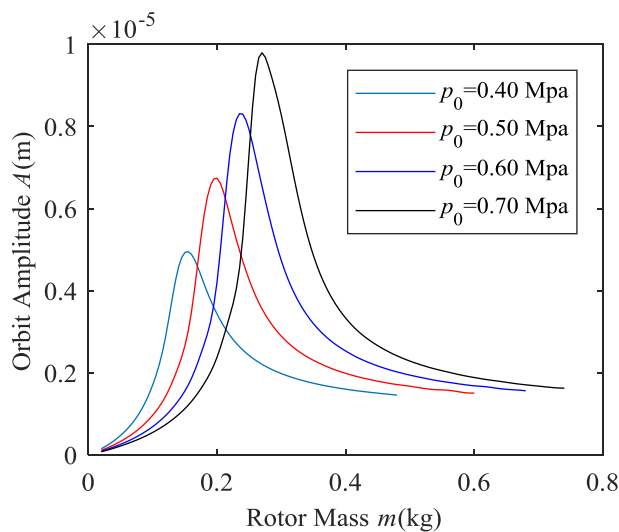

FIGURE 9. Variations of rotational accuracy with respect to the rotor mass less than threshold mass of instability (m_t) for different supply pressures.

is mainly due to the fact that the stiffness increases with supply pressure [38] and according to the condition that the

resonance occurs ($\sqrt{k/m} = \omega$), the larger the stiffness, the bigger the mass which corresponds to the resonance (m_r) is under constant angular speed. However, with the supply pressure growing, the amplitude at the resonance increases obviously. In addition, the influence of the supply pressure on rotational accuracy may be different at different rotor masses. It is found from Fig. 9 that before the resonance occurs (the rotor mass $m < m_r$), the orbit amplitude decreases with the increasing supply pressure. For instance, at $m = 0.1$ kg, the orbit amplitude reduces from 1.7 μm to 0.55 μm with the supply pressure increasing from 0.4 Mpa to 0.7 Mpa. On the other hand, for the large rotor mass beyond the m_r, the influence of supply pressure on the orbit amplitude is opposite of that for the rotor mass smaller than the m_r, which is clearly seen from Fig. 9.

Fig. 10 plots the stability maps for different supply pressures by showing the variations of the threshold mass of instability (m_t) with respect to the angular speeds of the rotor under different supply pressures. It can be seen that the curves are linear in the logarithmic coordinate system at all the supply pressures. With the growth of the angular speed, there is an obvious decrease in m_t. In addition, it can be seen
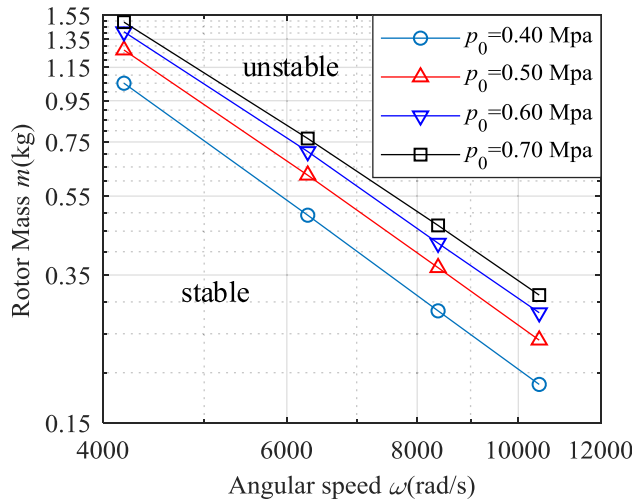
T. Yin *et al.*: Nonlinear Analysis of Stability and Rotational Accuracy of Unbalanced Rotor Supported by Aerostatic Journal Bearings

IEEE *Access*

FIGURE 10. Stability maps for different supply pressures.

FIGURE 11. Variations of rotational accuracy with respect to the rotor mass less than threshold mass of instability (m_t) for different orifice diameters.

that the increasing supply pressure leads to the increase of m_t, which means that the stability region is extended.

The effects of supply pressures on the dynamic behavior of the aerostatic bearing rotor system were experimentally investigated by increasing the angular speeds of the rotor in [39], [40], where the vibration amplitude increased first and then decreased until the threshold speed of instability. Thus, the angular speed plays a similar role with the rotor mass in the dynamic behavior of the rotor, although the relationship between the resonance speed and the threshold speed of instability is quite different from that between the m_r and m_t found in this study. Furthermore, it was found from [39], [40] that the influence of supply pressure on the vibration amplitudes was different at different angular speeds and the increasing supply pressure could lead to an increase in the instability threshold, which are similar to the results of this study. This validates the findings of this study to some extent.

The bearing length is also a geometric parameter affecting the dynamic response of the bearing-rotor system. The increasing bearing length can lead to an increase in the lubrication area and consequently increase the bearing forces, which is similar to the effect of supply pressure on the bearing forces. As a result, the bearing length has similar effects on the rotational accuracy and the threshold mass of instability as the supply pressure.

C. EFFECTS OF ORIFICE DIAMETER
The effects of orifice diameter on rotational accuracy, the resonance and instability threshold of the rotor are investigated. In the simulations, supply pressure $p_0 = 0.5$ Mpa, bearing clearance $h_0 = 20$ μm, and eccentric distance $r = 1$ μm.

The variations of rotational accuracy with respect to the rotor mass less than the threshold mass of instability (m_t) for different orifice diameters are presented in Fig. 11. The size of the orifice affects air flow and consequently the bearing's dynamic and static performance. The stiffness increases and
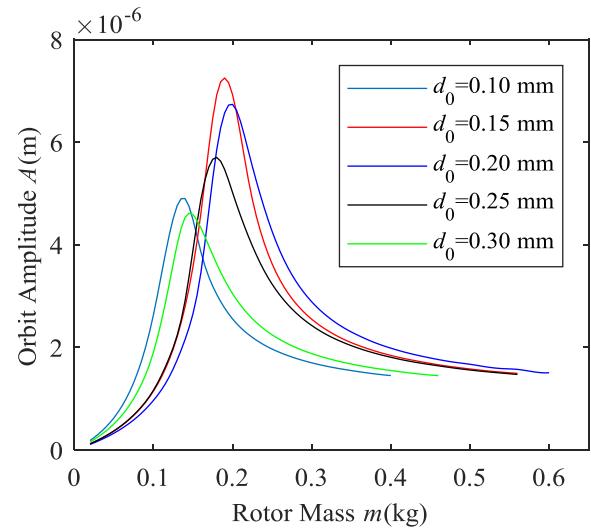
then decreases with the orifice diameter increase and according to the former analysis, the mass where the resonance occurs (m_r) should also increase first and then decrease, which can be clearly seen in Fig. 11. The orifice diameter also has a similar effect on the orbit amplitude at the resonance. The orifice diameter has a different influence on the rotational accuracy at different rotor masses. For the small rotor mass below the m_r, the orbit amplitude reduces first and then grows with the orifice diameter increase. However, the orifice diameter has an opposite effect on the orbit amplitude for a large rotor mass beyond the m_r. Fig. 12 shows the stability maps for different orifice diameters. It is shown that with the increasing orifice diameter, the value of the threshold mass of instability increases first and then decreases, which is in accordance with the trend of m_r. Therefore, there is an optimum value for the orifice diameter to achieve better rotational accuracy and stability.

D. EFFECTS OF BEARING CLEARANCE
In the aerostatic journal bearing rotor system, the rotor is supported by a thin air film between the bearing surface and rotor surface, and the dynamic performance of the bearing is strongly affected by the air film thickness. Thus, the bearing clearance is an important design parameter for the air bearing rotor system. The effects of bearing clearance on rotational accuracy, the resonance and instability threshold are studied. In the calculations, supply pressure $p_0 = 0.5$ Mpa, orifice diameter $d_0 = 0.2$ mm, and eccentric distance $r = 1$ μm.

Fig. 13 shows the variations of rotational accuracy with respect to the rotor mass less than the threshold mass of instability for different bearing clearance. It is shown that with the bearing clearance decreasing, the resonance can be delayed and the orbit amplitude at the resonance decreases. However, the resonance may appear earlier if the bearing clearance is too small (14 μm), this is mainly because there
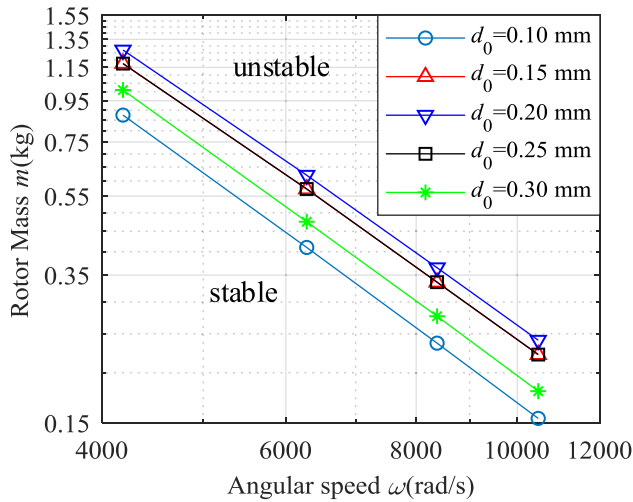
IEEE *Access*

T. Yin *et al.*: Nonlinear Analysis of Stability and Rotational Accuracy of Unbalanced Rotor Supported by Aerostatic Journal Bearings

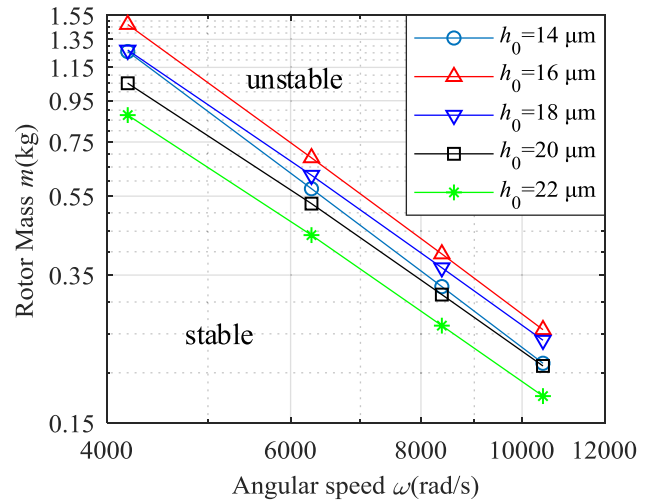**FIGURE 12.** Stability maps for different orifice diameters.

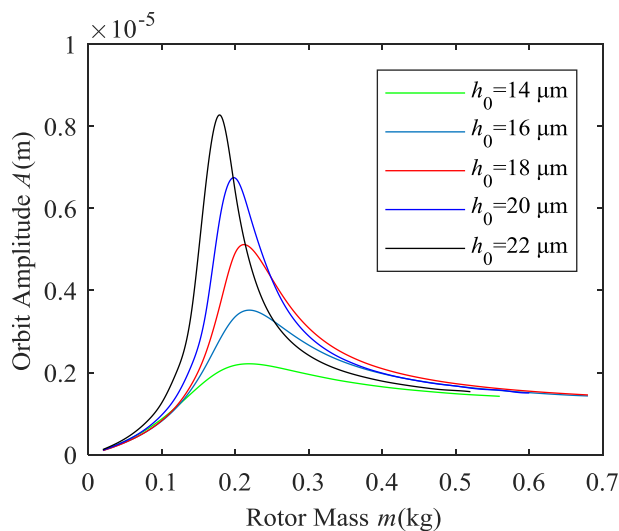**FIGURE 14.** Stability maps for different bearing clearance.

FIGURE 13. Variations of rotational accuracy with respect to the rotor mass less than threshold mass of instability (m_t) for different bearing clearance.

FIGURE 15. Variations of rotational accuracy with respect to the rotor mass less than threshold mass of instability (m_t) for different eccentric distances.

is not enough air to support the rotor, resulting in low bearing stiffness. For a small rotor mass below the m_r, the decreasing bearing clearance leads to a smaller orbit amplitude, but the amplitude shows a slight increase in the case of the bearing clearance $h_0 = 14$ μm. On the other hand, for a large rotor mass beyond the m_r, the influence of the bearing clearance on the orbit amplitude is different. The amplitude increases first and then decreases with the bearing clearance decreasing and is at its minimum at the bearing clearance of 14 μm. Fig. 14 shows the stability maps for different bearing clearance. It can be seen that with the decreasing bearing clearance, m_t increases, but it shows a decrease at $h_0 = 14$ μm. Similar with the orifice diameter, there also exists an optimum value for the bearing clearance to achieve better rotational accuracy and stability. Thus, the bearing clearance should be selected carefully when designing the bearing rotor system.
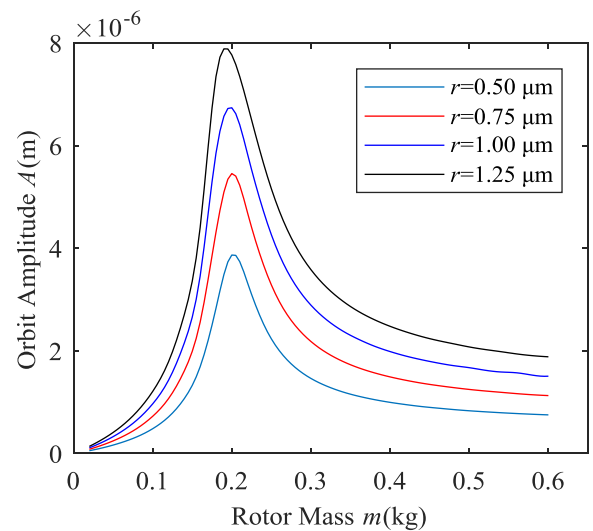
E. EFFECTS OF ECCENTRIC DISTANCES

The effects of eccentric distances on rotational accuracy, the resonance and instability threshold are investigated. In the calculations, supply pressure $p_0 = 0.5$ Mpa, bearing clearance $h_0 = 20$ μm, and orifice diameter $d_0 = 0.2$ mm.

The variations of rotational accuracy with respect to the rotor mass less than the threshold mass of instability for different eccentric distances are described in Fig. 15. It is shown that the mass which corresponds to the resonance (m_r) decreases very slightly with the eccentric distance increasing, which is probably due to the fact that the stiffness decreases with the increasing distance between the rotor's center and the bearing center [37]. Unlike supply pressure, orifice diameter and bearing clearance, the eccentric distance has the same effect on the orbit amplitude for the whole rotor mass range. It is clearly seen that the amplitude increases proportionally with the eccentric distances, which is consistent with the
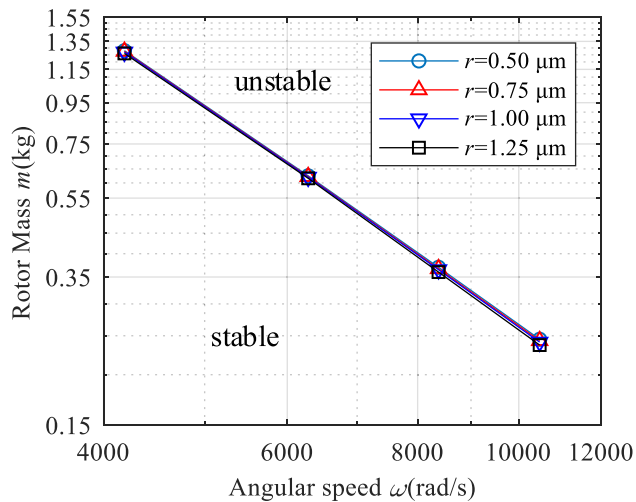
T. Yin *et al.*: Nonlinear Analysis of Stability and Rotational Accuracy of Unbalanced Rotor Supported by Aerostatic Journal Bearings

IEEE *Access*

FIGURE 16. Stability maps for different eccentric distances.

results from [39]. Fig. 16. shows stability maps for different eccentric distances. The threshold mass of instability (m_t) has little dependence on the eccentric distances, which indicates that the half frequency whirl instability is self-excited and not influenced by the mass unbalance.

IV. CONCLUSION

In this paper, the nonlinear dynamic response of an aerostatic bearing with an unbalanced rotor is studied. Under the same operating speed, the rotor mass where the resonance occurs (m_r) is investigated, and its relationship with the mass at the threshold of instability (m_t) is found for the first time. And the influence of supply pressure, orifice diameter, bearing clearance, and eccentric distance on the rotational accuracy, resonance and instability threshold are numerically studied. This study offers guidance for designing the aerostatic bearing rotor systems. The study's conclusions are summarized as follows.

1) The dynamic responses of an unbalanced rotor supported by aerostatic bearings strongly depend on the rotor mass. The periodic, multi-periodic or quasi-periodic motions occur as the rotor mass changes.

2) With the growth of the rotor mass, the orbit amplitude increases until the resonance occurs and then decreases until the m_t, which is nearly 4 times the m_r. After the m_t, half frequency whirl occurs and the amplitude grows dramatically, which means the rotor is unstable. Besides, the variation curve of m_t with the angular speed is linear in the logarithmic coordinate system.

3) With increasing supply pressure, the m_r and m_t increase, although there is also an obvious increase in the orbit amplitude at the resonance. The influence of the supply pressure on rotational accuracy is different at different rotor masses. At the small rotor mass below the m_r, the bigger supply pressure leads to the smaller orbit amplitude, although the effect of supply pressure

on the orbit amplitude is opposite at the large rotor mass above the m_r.

4) As the orifice diameter or bearing clearance increases, the m_r and m_t and the orbit amplitude at the resonance increase first and then decrease. And the orbit amplitude at the rotor mass below the m_r decreases first and then increases. The orifice diameter or bearing clearance has the opposite effect on rotational accuracy at the large rotor mass above the m_r.

5) The m_r and m_t have little dependence on the eccentric distance. The increasing eccentric distance can result in a bigger orbit amplitude for the whole rotor mass range.

REFERENCES

[1] B. Yang, S. Feng, J. Tian, and L. Yu, "Investigation on the nonlinear dynamic characteristics of the air lubricated bearing concerning frequency of perturbation effect," in *Proc. IEEE Int. Conf. Mechatronics Autom. (ICMA)*, Aug. 2019, pp. 1230–1235.

[2] Z. Tang, D. Zhou, T. Jia, X. Zhang, and D. Pan, "Effect of air bearing pressure and slider/disk contact on lubricant depletion using molecular dynamics simulation," *IEEE Trans. Magn.*, vol. 56, no. 4, Apr. 2020, Art. no. 6702804.

[3] D. Wu, B. Wang, X. Luo, and Z. Qiao, "Design and analysis of aerostatic spindle with high load characteristics for large ultra-precision drum lathe," *Proc. Inst. Mech. Eng., J, J. Eng. Tribol.*, vol. 229, no. 12, pp. 1425–1434, Dec. 2015.

[4] S. J. Zhang, S. To, and H. T. Wang, "A theoretical and experimental investigation into five-DOF dynamic characteristics of an aerostatic bearing spindle in ultra-precision diamond turning," *Int. J. Mach. Tools Manuf.*, vol. 71, pp. 1–10, Aug. 2013.

[5] V. Castelli and H. G. Elrod, "Solution of the stability problem for 360 deg self-acting, gas-lubricated bearings," *J. Basic Eng.*, vol. 87, no. 1, pp. 199–210, Mar. 1965.

[6] N. Vlajic, A. R. Champneys, and B. Balachandran, "Nonlinear dynamics of a Jeffcott rotor with torsional deformations and rotor-stator contact," *Int. J. Non-Linear Mech.*, vol. 92, pp. 102–110, Jun. 2017.

[7] P. Huang, W. B. Lee, and C. Y. Chan, "Investigation of the effects of spindle unbalance induced error motion on machining accuracy in ultra-precision diamond turning," *Int. J. Mach. Tools Manuf.*, vol. 94, pp. 48–56, Jul. 2015.

[8] N. Vlajic, X. Liu, H. Karki, and B. Balachandran, "Torsional oscillations of a rotor with continuous stator contact," *Int. J. Mech. Sci.*, vol. 83, pp. 65–75, Jun. 2014.

[9] J. S. Ausman, "Linearized ph stability theory for translatory half-speed whirl of long, self-acting gas-lubricated journal bearings," *J. Basic Eng.*, vol. 85, no. 4, pp. 611–618, Dec. 1963.

[10] J. W. Lund, "Calculation of stiffness and damping properties of gas bearings," *J. Lubrication Technol.*, vol. 90, no. 4, pp. 793–803, Oct. 1968.

[11] Y. Lihua, Q. Shemiao, and Y. Lie, "Numerical analysis on dynamic coefficients of self-acting gas-lubricated tilting-pad journal bearings," *J. Tribol.*, vol. 130, no. 1, Jan. 2008, Art. no. 011006.

[12] F. Al-Bender, "On the modelling of the dynamic characteristics of aerostatic bearing films: From stability analysis to active compensation," *Precis. Eng.*, vol. 33, no. 2, pp. 117–126, Apr. 2009.

[13] C.-H. Chen, T.-H. Tsai, D.-W. Yang, Y. Kang, and J.-H. Chen, "The comparison in stability of rotor-aerostatic bearing system compensated by orifices and inherences," *Tribol. Int.*, vol. 43, no. 8, pp. 1360–1373, Aug. 2010.

[14] P. Yu, X. Chen, X. Wang, and W. Jiang, "Frequency-dependent nonlinear dynamic stiffness of aerostatic bearings subjected to external perturbations," *Int. J. Precis. Eng. Manuf.*, vol. 16, no. 8, pp. 1771–1777, Jul. 2015.

[15] Y. Chang, "Stability boundary of non-linear orbits within clearance circle of journal bearings," *J. Vib. Acoust.*, vol. 115, no. 3, p. 303, Jul. 1993.

[16] A. K. Tieu and Z. L. Qiu, "Stability of finite journal bearings—From linear and nonlinear bearing forces," *Tribol. Trans.*, vol. 38, no. 3, pp. 627–635, Jan. 1995.

[17] F. Colombo, T. Raparelli, and V. Viktorov, "Externally pressurized gas bearings: A comparison between two supply holes configurations," *Tribol. Int.*, vol. 42, no. 2, pp. 303–310, Feb. 2009.

IEEE Access

T. Yin *et al.*: Nonlinear Analysis of Stability and Rotational Accuracy of Unbalanced Rotor Supported by Aerostatic Journal Bearings

[18] C.-C. Wang and H.-T. Yau, "Theoretical analysis of high speed spindle air bearings by a hybrid numerical method," *Appl. Math. Comput.*, vol. 217, no. 5, pp. 2084–2096, Nov. 2010.

[19] P.-H. Kuo, R.-M. Lee, and C.-C. Wang, "A high-precision random forest-based maximum Lyapunov exponent prediction model for spherical porous gas bearing systems," *IEEE Access*, vol. 8, pp. 168079–168086, 2020.

[20] D. L. Martin, A. N. Tabenkin, and F. G. Parsons, "Precision spindle and bearing error analysis," *Int. J. Mach. Tools Manuf.*, vol. 35, no. 2, pp. 187–193, Feb. 1995.

[21] E. R. Marsh, D. A. Arneson, and D. L. Martin, "A comparison of reversal and multiprobe error separation," *Precis. Eng.*, vol. 34, no. 1, pp. 85–91, Jan. 2010.

[22] E. Marsh, J. Couey, and R. Vallance, "Nanometer-level comparison of three spindle error motion separation techniques," *J. Manuf. Sci. Eng.*, vol. 128, no. 1, pp. 180–187, Feb. 2006.

[23] S. Shi, J. Lin, X. Wang, and M. Zhao, "A hybrid three-probe method for measuring the roundness error and the spindle error," *Precis. Eng.*, vol. 45, pp. 403–413, Jul. 2016.

[24] S. Cappa, D. Reynaerts, and F. Al-Bender, "A sub-nanometre spindle error motion separation technique," *Precis. Eng.*, vol. 38, no. 3, pp. 458–471, Jul. 2014.

[25] K.-M. Kim and K.-W. Kim, "An analytical study on the rotational accuracy of externally pressurized air journal bearing," *Int. J. Vib., Control Eng., Eng. Ind.*, vol. 35, no. 3, pp. 485–492, 1992.

[26] D.-C. Han, S.-S. Park, W.-J. Kim, and J.-W. Kim, "A study on the characteristics of externally pressurized air bearings," *Precis. Eng.*, vol. 16, no. 3, pp. 164–173, Jul. 1994.

[27] H. Yabe, "A study on run-out characteristics of externally pressurized gas journal bearing: Modified DF method for point-source solution," *Int. J. C, Dyn., Control, Robot., Des. Manuf.*, vol. 37, no. 2, pp. 362–368, 1994.

[28] H. Yabe, "A study on run-out characteristics of externally pressurized gas journal bearing: Rotor run-out characteristics," *Int. J. C, Dyn., Control, Robot., Des. Manuf.*, vol. 37, no. 2, pp. 355–361, 1994.

[29] S. Cappa, D. Reynaerts, and F. Al-Bender, "Reducing the radial error motion of an aerostatic journal bearing to a nanometre level: Theoretical modelling," *Tribol. Lett.*, vol. 53, no. 1, pp. 27–41, Jan. 2014.

[30] H. Cui, Y. Wang, X. Yue, M. Huang, W. Wang, and Z. Jiang, "Numerical analysis and experimental investigation into the effects of manufacturing errors on the running accuracy of the aerostatic porous spindle," *Tribol. Int.*, vol. 118, pp. 20–36, Feb. 2018.

[31] P. Yang, K.-Q. Zhu, and X.-L. Wang, "On the non-linear stability of self-acting gas journal bearings," *Tribol. Int.*, vol. 42, no. 1, pp. 71–76, Jan. 2009.

[32] D. Tan and Z. Chen, "On a general formula of fourth order Runge-Kutta method," *J. Math. Sci. Math. Educ.*, vol. 7, no. 2, pp. 1–10, 2012.

[33] Z. Guo, Y. Cao, K. Feng, H. Guan, and T. Zhang, "Effects of static and imbalance loads on nonlinear response of rigid rotor supported on gas foil bearings," *Mech. Syst. Signal Process.*, vol. 133, Nov. 2019, Art. no. 106271.

[34] Z. Guo, K. Feng, T. Liu, P. Lyu, and T. Zhang, "Nonlinear dynamic analysis of rigid rotor supported by gas foil bearings: Effects of gas film and foil structure on subsynchronous vibrations," *Mech. Syst. Signal Process.*, vol. 107, pp. 549–566, Jul. 2018.

[35] D. Liu, Y. Liu, and S. Chen, *Aerostatic Lubrication*. Harbin, China: Harbin Institute of Technology Press, 1990.

[36] Y. Xiaoni and P. Xudong, "Selection of a shape function in finite element analysis for a spiral groove dry gas seal," *Lubrication Eng.-Huangpu*, vol. 3, no. 175, p. 13, 2006.

[37] J. Du, G. Zhang, T. Liu, and S. To, "Improvement on load performance of externally pressurized gas journal bearings by opening pressure-equalizing grooves," *Tribol. Int.*, vol. 73, pp. 156–166, May 2014.

[38] H. Xiao, W. Li, Z. Zhou, X. Huang, and Y. Ren, "Performance analysis of aerostatic journal micro-bearing and its application to high-speed precision micro-spindles," *Tribol. Int.*, vol. 120, pp. 476–490, Apr. 2018.

[39] D. A. Frew and C. Scheffer, "Numerical modelling of a high-speed rigid rotor in a single-aerostatic bearing using modified euler equations of motion," *Mech. Syst. Signal Process.*, vol. 22, no. 1, pp. 133–154, Jan. 2008.

[40] L. S. Andrés and K. Ryu, "Hybrid gas bearings with controlled supply pressure to eliminate rotor vibrations while crossing system critical speeds," *J. Eng. Gas Turbines Power*, vol. 130, no. 6, Nov. 2008, Art. no. 062505.

TENGFEI YIN received the B.Eng. degree in mechanical engineering from the China University of Mining and Technology, in 2014, and the M.Eng. degree in mechanical engineering from the Harbin Institute of Technology, in 2017. He is currently pursuing the Ph.D. degree with the Department of Industrial and System Engineering, The Hong Kong Polytechnic University. His research interests include rotor dynamics and ultraprecision machining technology.

GUOQING ZHANG received the M.Eng. degree in mechanical engineering from the Harbin Institute of Technology, in 2009, and the Ph.D. degree in advanced manufacturing technology from The Hong Kong Polytechnic University, in 2014. He is currently a Professor with Shenzhen University. His research interests include ultraprecision machining technology, robots, and intelligent equipment.

JIANJUN DU received the B.S. and M.S. degrees from Liaoning Technical University, China, in 1996 and 1999, respectively, and the Ph.D. degree in mechanical engineering from the Harbin Institute of Technology, China, in 2002. He is currently a Professor with the Harbin Institute of Technology at Shenzhen, Shenzhen, China. His research interests include precision mechanical designs, dynamic and control of mobile robot (lunar rover), and machine vision and visual servoing of robot. He is the Chairman of the Gas Lubrication Committee of the Tribology Institute of Chinese Mechanical Engineering Society.

SUET TO (Member, IEEE) received the M.Phil. degree in material science from Brunel University London, London, U.K., in 1993, and the Ph.D. degree in ultraprecision machining technology from The Hong Kong Polytechnic University, Hong Kong, in 2000.

She is currently a Professor with the Department of Industrial and Systems Engineering, The Hong Kong Polytechnic University, where she is also the Associate Director of the State Key Laboratory of Ultraprecision Machining Technology and the Advanced Optics Manufacturing Centre. She is an Active Researcher, who focuses on industry-related and applied research in ultraprecision machining, advanced optics manufacturing, and precision injection molding and material science.

• • •